Article

Structural basis of ketamine action on human NMDA receptors

Youyi Zhang[1,2,7], Fei Ye[3,7], Tongtong Zhang[1,2,7], Shiyun Lv[1,2], Liping Zhou[2,4], Daohai Du[4], He Lin[5], Fei Guo[4], Cheng Luo[2,4✉] & Shujia Zhu[1,2,6✉]

Ketamine is a non-competitive channel blocker of N-methyl-D-aspartate (NMDA) receptors[1]. A single sub-anaesthetic dose of ketamine produces rapid (within hours) and long-lasting antidepressant effects in patients who are resistant to other antidepressants[2,3]. Ketamine is a racemic mixture containing equal parts of (R)- and (S)-ketamine, with the (S)-enantiomer having greater affinity for the NMDA receptor[4]. Here we describe the cryo-electron microscope structures of human GluN1–GluN2A and GluN1–GluN2B NMDA receptors in complex with S-ketamine, glycine and glutamate. Both electron density maps uncovered the binding pocket for S-ketamine in the central vestibule between the channel gate and selectivity filter. Molecular dynamics simulation showed that S-ketamine moves between two distinct locations within the binding pocket. Two amino acids—leucine 642 on GluN2A (homologous to leucine 643 on GluN2B) and asparagine 616 on GluN1—were identified as key residues that form hydrophobic and hydrogen-bond interactions with ketamine, and mutations at these residues reduced the potency of ketamine in blocking NMDA receptor channel activity. These findings show structurally how ketamine binds to and acts on human NMDA receptors, and pave the way for the future development of ketamine-based antidepressants.

Major depressive disorder affects about 6–16% of the global population[5]. Conventional antidepressants that target the monoaminergic system typically take weeks to produce effects and are ineffective in one-third of patients[6]. Recently, the enantiomer S-ketamine was approved by the US Food and Drug Administration as the first non-monoaminergic drug for treatment-resistant major depressive disorder[7]. In clinical studies, ketamine quickly reduces the core symptoms of depression and suicidal ideation[2,8]. Laboratory studies have shown that ketamine rapidly ameliorates depressive mood by blocking NMDA receptor-dependent activities[9], and reverses stress-induced loss of neuronal spines and circuit dysfunctions[10,11]. In this study, we determined the cryo-electron microscope (cryo-EM) structures of ketamine-bound human GluN1–GluN2A and GluN1–GluN2B channels—two major subtypes of NMDA receptor in the adult brain.

NMDA receptors are glutamate-gated calcium-permeable ion channels that have pivotal roles in synaptic transmission and plasticity, which are essential for learning and memory. Functional NMDA receptors usually form heterotetrameric complexes comprising two glycine-bound GluN1 subunits and two glutamate-bound GluN2 (2A–2D) subunits[12]. Previous studies[13–16] have shown that truncation of the C-terminal domains (CTDs) of both GluN1 and GluN2 subunits is required for detergent-solubilized NMDA receptors to be thermostable in vitro. We constructed and expressed recombinant CTD-truncated (denoted by EM) GluN1–GluN2A$_{EM}$ or GluN1–GluN2B$_{EM}$ NMDA receptors

in a mammalian expression system, and purified monodisperse proteins with the expected profiles of tetrameric assembly (Extended Data Fig. 1a, b). Two-electrode voltage-clamp (TEVC) recordings and binding assays verified that the affinity and efficacy of ketamine were normal for both GluN1–GluN2A$_{EM}$ and GluN1–GluN2B$_{EM}$ receptors (Fig. 1f, Extended Data Fig. 1c, d). These data ensured S-ketamine occupancy within both receptors.

To trap the NMDA receptors in the ketamine-bound state, we pre-incubated the purified protein with glycine and glutamate (1 mM each) in the presence of S-ketamine (5 mM), which is 3–5 times more potent than R-ketamine[17]. Next, we vitrified the protein and collected the structural data sets using cryo-EM. No symmetry was applied during the data processing. The final 3D refinement yielded density maps of GluN1–GluN2A and GluN1–GluN2B receptors at nominal global resolutions of 3.5 Å and 4.0 Å, respectively (Fig. 1a, b, Extended Data Fig. 2, Extended Data Table 1). In agreement with previously reported structures[13–16], human GluN1–GluN2A and GluN1–GluN2B receptors adopted the configuration of typical heterotetramers with extracellular N-terminal domains (NTDs) and ligand-binding domains (LBDs), as well as a transmembrane domain (TMD) embedded in the lipid bilayer (Fig. 1a, b). The cryo-EM map of the GluN1–GluN2A receptor revealed the EM densities for the agonists glycine and glutamate (Extended Data Fig. 3a, b). The resolution of the EM density in the entire extracellular region went beyond 3 Å, allowing the placement of the majority of

[1]Institute of Neuroscience, State Key Laboratory of Neuroscience, CAS Center for Excellence in Brain Science and Intelligence Technology, Chinese Academy of Sciences, Shanghai, China. [2]University of Chinese Academy of Sciences, Beijing, China. [3]College of Life Sciences and Medicine, Zhejiang Sci-Tech University, Hangzhou, China. [4]Drug Discovery and Design Center, the Center for Chemical Biology, State Key Laboratory of Drug Research, Shanghai Institute of Materia Medica, Chinese Academy of Sciences, Shanghai, China. [5]Criminal Investigation Technology Department, The Third Research Institute of Ministry of Public Security, Shanghai, China. [6]Shanghai Center for Brain Science and Brain-Inspired Intelligence Technology, Shanghai, China. [7]These authors contributed equally: Youyi Zhang, Fei Ye, Tongtong Zhang. ✉e-mail: cluo@simm.ac.cn; shujiazhu@ion.ac.cn
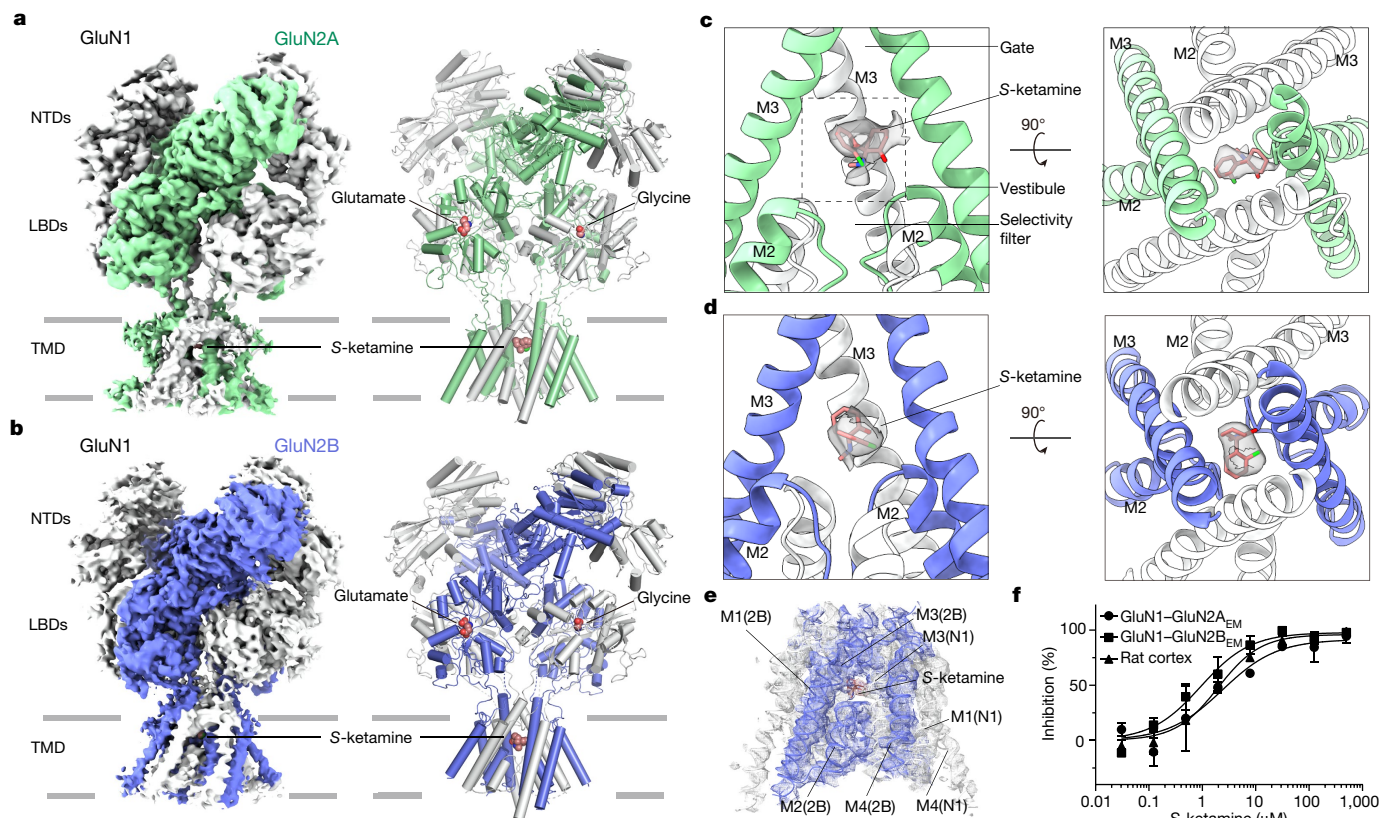
Fig. 1 | S-ketamine-bound cryo-EM structures of human GluN1–GluN2A and GluN1–GluN2B NMDA receptors. a, **b**, Cryo-EM densities (left) and structural models (right) of human GluN1–GluN2A (**a**) and GluN1–GluN2B receptors (**b**). GluN1 subunits are represented in grey with glycine captured in the LBDs; GluN2A and GluN2B are represented in green and blue, respectively, with glutamate presented in the clefts. S-ketamine was captured within the TMD in both receptors. **c**, **d**, The TMDs of GluN1–GluN2A (**c**) and GluN1–GluN2B receptors (**d**) with side (left) and top-down views (right), showing the binding pocket of S-ketamine in the central vestibule, between the gate and selectivity filter. S-ketamine (in red stick form) was fitted with EM density (grey surface). **e**, Cryo-EM density (mesh) in the TMD region of the GluN1–GluN2B receptor (ribbon) and S-ketamine (red stick). 2B and N1 in parentheses denote the GluN2B and GluN1 subunits, respectively. **f**, Displacement of [^{3}H]MK-801 for S-ketamine in GluN1–GluN2A$_{EM}$ (inhibitory constant, $K_i = 1.22 \pm 0.39$ μM), GluN1–GluN2B$_{EM}$ receptors ($K_i = 0.68 \pm 0.18$ μM) and rat cortex tissue ($K_i = 1.11 \pm 0.16$ μM). Mean ± s.e.m. from triplicate measurements.

amino acids in NTDs, LBDs and NTD–LBD linkers, as well as of glycosylation modifications (Extended Data Fig. 3c, d). However, the overall density in the TMD of GluN1–GluN2A receptor was less well resolved, presumably because of the dynamic conformational changes associated with the fast channel kinetics of GluN1–GluN2A receptors[12,18]. By contrast, the TMD density in GluN1–GluN2B receptors was much better resolved, allowing fitting of most residues to the density map (Fig. 1e, Extended Data Fig. 2f).

Notably, we found an EM density for the trapped S-ketamine within the TMD region in both GluN1–GluN2A and GluN1–GluN2B receptors. The TMD is composed of three α-helical transmembrane segments (M1, M3 and M4) and a short re-entrant loop (M2) from each subunit, with the ion channel gate at the top, the selectivity filter at the bottom and the vestibule in between (Fig. 1c, d). The structures of both GluN1–GluN2A and GluN1–GluN2B receptors confirmed the presence of the binding pocket of S-ketamine within the central vestibule. The local resolution of the electron density was not sufficient to perfectly fit the geometry of S-ketamine, presumably owing to the dynamic occupancy of the ligand, as indicated by the molecular dynamics (MD) simulation described below. As the pyramidal vestibule consists of a polar bottom mainly contributed by the 'QRN' site[19] (where the residue (glutamine, arginine or asparagine) at the tip of the pore loop is edited by RNA splicing) and a hydrophobic pouch formed by the M3 helices, we fitted the density map with the amino-group of ketamine pointing to the hydrophilic QRN site and its aromatic rings facing up to the hydrophobic pouch (Fig. 1c, d).

MD simulations have been used for studies of channel blockers[20], allostery mechanisms[21] and cross-subunit interactions[22] in NMDA receptors. To gain more insights into binding of S-ketamine, we carried out an MD simulation with the S-ketamine bound TMD of the GluN1–GluN2A receptor as the initial structure. The MD results showed large fluctuations of the S-ketamine during a 500-ns simulation (Fig. 2a), which suggests that the localization of this molecule within its binding environment is highly dynamic. We used the root-mean-square deviation (r.m.s.d.) values to cluster the distribution of S-ketamine into two distinct upper and lower poses (Fig. 2b). Beginning from about 200 ns into the simulation, S-ketamine gradually pointed towards the selectivity filter in the lower pose. From about 350 ns, S-ketamine moved up to the upper pose closer to that in the initial cryo-EM state (Fig. 2a–c, Supplementary Video 1). Accordingly, we propose that the cryo-EM structure captured one of the predominant upper binding poses, while the others were intermediate states.

To further understand the contributions of individual residues within the TMD to S-ketamine binding, we performed per-residue decomposition studies of relative binding energy based on MD simulation using the MM-PBSA method (excluding entropic contribution). We analysed the contributions of residues within 10 Å of S-ketamine (Fig. 2d). Among these amino acids, Leu642 in both GluN2A subunits, which formed extensive hydrophobic interactions with S-ketamine, made the most substantial contribution to relative binding energy (−4.74 and −2.28 kJ mol⁻¹ in two GluN2A protomers, respectively). In addition, Asn616 in one GluN1 protomer was also crucial for binding
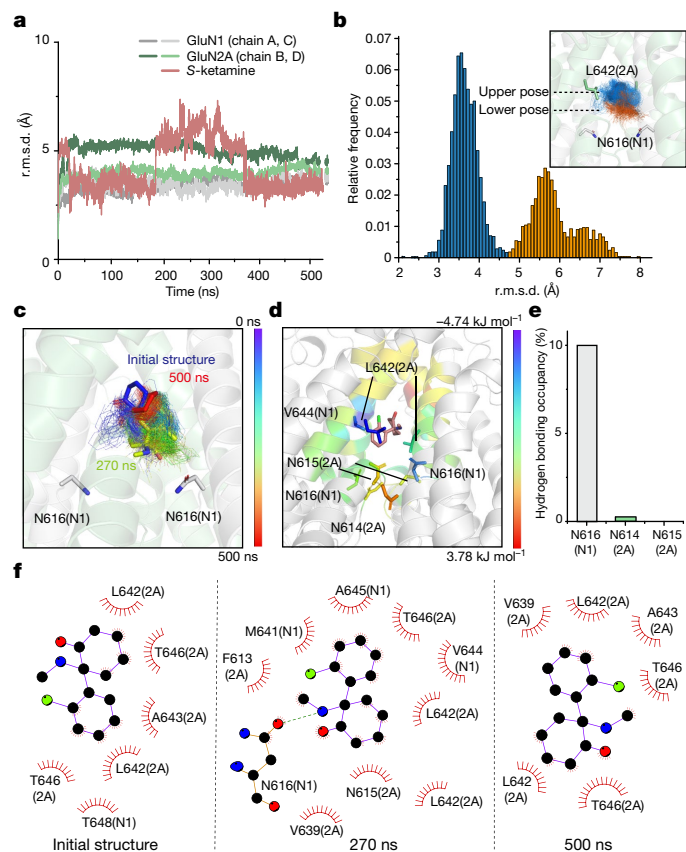
Fig. 2 | MD simulation of the S-ketamine-bound TMD of the GluN1–GluN2A receptor. a, r.m.s.d. trajectories for each chain (excluding M1–M2 loops) of TMD and *S*-ketamine calculated on Cα atoms based on the initial structure within the total simulation time of 500 ns. **b**, Two predominant poses of *S*-ketamine obtained in the MD simulation owing to the distribution of the r.m.s.d.s of *S*-ketamine. **c**, *S*-ketamine poses obtained in MD simulation during the total simulation time. **d**, Per-residue decomposition of relative binding energy for residues within 10 Å of *S*-ketamine. **e**, Occupancy of hydrogen bonds between *S*-ketamine and the QRN site residues in the selectivity filter from 230 ns to 310 ns during the MD simulation. **f**, Schematic showing ligand–protein interactions of different snapshots extracted from MD simulation (initial structure, 270 ns, and 500 ns). Residues involved in hydrophobic interactions are shown as starbursts, and hydrogen-bonding interactions are denoted by dotted green lines.

of *S*-ketamine (−3.67 kJ mol⁻¹) (Extended Data Table 2). Ligplot⁺ analysis revealed that *S*-ketamine interacted with Leu642 of GluN2A through strong hydrophobic interactions in all configurations (Fig. 2f), while its secondary amine formed a hydrogen bond with the polar Asn616 of GluN1 (but not with Asn614 or Asn615 of GluN2A) in the selectivity filter in the lower pose captured by MD simulation (Fig. 2c–e). These in silico results implied that Asn616 of GluN1 and Leu642 of GluN2A had crucial roles in maintaining the binding of *S*-ketamine.

Next, we performed TEVC recordings to examine the ketamine-induced inhibition of current in human GluN1–GluN2A receptors. It has previously been reported that the QRN sites are responsible for binding the pore blockers Mg²⁺, MK-801 and memantine[19,20,23]. In line with our simulation data, we found that ketamine inhibition was essentially abolished in GluN1(N616A)–GluN2A receptors, in which Asn616 of GluN1 is replaced with an alanine, which has a short nonpolar side chain (Fig. 3a, c). Moreover, GluN1(N616Q)–GluN2A channels, in which Asn616 was mutated to glutamine (which has a longer side chain but the same polarity), also showed a marked (42-fold) reduction in inhibition by ketamine (Fig. 3c, Extended Data Table 3). This implied that the hydrogen bonding between N616 and ketamine was steric-sensitive.

By contrast, alanine substitutions at the QRN site (Asn614) and the adjacent N+1 site (Asn615) in the GluN2A subunit had minimum effects on inhibition by *S*-ketamine (Extended Data Fig. 5d, g), consistent with the calculations of hydrogen bonding propensity and energy decomposition in our MD simulation (Fig. 2e).

Subsequently, we mutated Leu642 of GluN2A in the vestibule pouch to other aliphatic amino acids. Isoleucine and valine substitutions reduced the potency of inhibition by ketamine by four- and seven-fold, respectively, whereas alanine and glycine substitutions produced stronger reductions (approximately 50- and 100-fold, respectively) (Fig. 3d, Extended Data Table 3). Notably, plotting the half-maximal inhibitory concentration (IC₅₀) of ketamine against the residue volume at the Leu642 position showed a linear regression fit ($R^2 = 0.92$), indicating that these hydrophobic interactions were highly steric-sensitive (Fig. 3e). These data are consistent with the structural information that the non-polar side chain of leucine formed strong hydrophobic interactions with the 2-chlorophenyl and cyclohexanone groups of ketamine (Fig. 3a). Furthermore, when the leucine was substituted with the polar asparagine, the GluN1–GluN2A(L642N) receptors displayed a greater reduction in ketamine potency (Fig. 3f). Current–voltage curves indicated that the magnesium block was not disrupted in any of these mutant receptors (Extended Data Fig. 4a). Notably, the ClinVar database includes the human missense mutation c.1925T>G (L642R) in *GRIN2A*; receptors with this mutation (GluN1–GluN2A(L642R)) showed a nearly complete loss of ketamine sensitivity (Fig. 3f). Furthermore, homologous leucine on various GluN2B or GluN2D subunits also showed steric-sensitive hydrophobic interactions with ketamine (Extended Data Fig. 4b, c). Together, these data show that this conserved leucine in all GluN2 subunits is the dominant residue responsible for ketamine binding in various subtypes of NMDA receptors (Extended Data Fig. 6a).

As Val644 in GluN1 also formed hydrophobic interactions with ketamine in the MD simulation (Fig. 2d, f), we investigated the contribution of this residue to ketamine-mediated inhibition. Substitution of this residue with alanine (or leucine) produced a threefold decrease in ketamine sensitivity (Extended Data Fig. 4d). In addition, GluN1(V644T)–GluN2A receptors showed similar ketamine-mediated inhibition to wild-type receptors (Extended Data Fig. 4d). To rule out other possible ketamine-binding sites, we mutated Thr648 in GluN1 and Thr646 in GluN2A at the top of the central vestibule to valines. Both mutant receptors showed unaltered ketamine potency (Extended Data Fig. 5d).

Ligplot⁺ analysis of the *S*-ketamine-bound GluN1–GluN2B structure revealed that the hydrogen bond with Asn616 in GluN1 and the hydrophobic contacts with Leu643 in GluN2B are conserved in human GluN1–GluN2B receptors (Fig. 3b, Extended Data Fig. 4f). Dose–response curves showed that GluN1(N616A)–GluN2B and GluN1–GluN2B(L643A) receptors displayed more than 15-fold reductions in ketamine potency (Fig. 3g). We also investigated whether Val644 in GluN1 was involved in binding ketamine. TEVC data revealed that both GluN1(V644A)–GluN2B and GluN1(V644T)–GluN2B receptors showed twofold enhancement in inhibition by ketamine, whereas GluN1(V644L)–GluN2B receptors displayed unaltered ketamine potency (Extended Data Fig. 4e). These data indicated that the hydrophobic interaction contributed by the leucine residue (642 in GluN2A and 643 in GluN2B) was the predominant interaction with ketamine.

There is increasing preclinical evidence that *R*-ketamine may have longer-lasting antidepressant effects and fewer side effects than *S*-ketamine[17,24]. Therefore, we carried out MD simulations based on the *R*-ketamine-docked TMD of GluN1–GluN2A receptors. The simulations showed that *R*-ketamine reached a relatively stable position after moving towards the selectivity filter during the initial stage (Extended Data Fig. 5b, Supplementary Video 1). We further performed TEVC on mutated GluN1–GluN2A receptors to examine the differential effects of these two enantiomers. All mutations on Asn616 in GluN1 and Leu642 in GluN2A significantly reduced inhibition by both *R*- and *S*-ketamine, whereas the GluN1(T648V), GluN2A(T646V) and GluN2A(N615A)
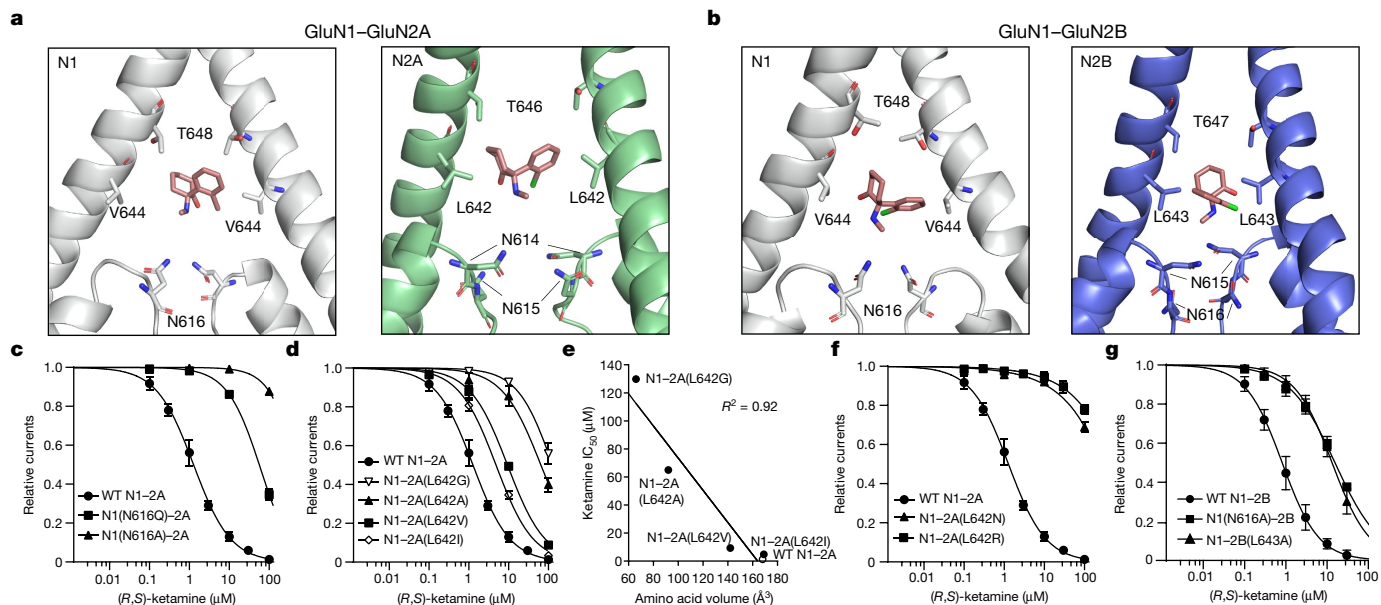
Fig. 3 | Mechanism by which ketamine inhibits GluN1–GluN2A and GluN1–GluN2B NMDA receptors. a, **b**, Structures of human GluN1–GluN2A TMD (**a**) and GluN1–GluN2B TMD (**b**), with residues surrounding the central vestibule shown as sticks. *S*-ketamine is represented in red stick form. **c**, **d**, (*R,S*)-ketamine dose–response curves (mean ± s.d.) for wild-type (WT) GluN1–GluN2A receptors and receptors incorporating substitution with A or Q at GluN1-N616 (**c**) or substitution with G, A, V or I at GluN2A-L642 (**d**). **e**, Plot of wild-type (open circle) and mutant (filled circles) amino acid volume at position GluN2A-L642 plotted against ketamine IC$_{50}$, showing a linear regression fit ($R^2 = 0.92$). **f**, (*R,S*)-ketamine dose–response curves (mean ± s.d.) for wild-type GluN1–GluN2A receptors and receptors with asparagine or arginine (human variant) substitutions at GluN2A-L642. **g**, (*R,S*)-ketamine dose–response curves (mean ± s.d.) for wild-type GluN1–GluN2B, GluN1(N616A)–GluN2B and GluN1–GluN2B(L643A) receptors. All data recorded at holding potential of −60 mV. IC$_{50}$ values, Hill slopes and numbers of oocytes are listed in Extended Data Table 3. Data were obtained from two independent experiments.

mutations had minimal effects (Extended Data Fig. 5a, d, e). Notably, substitutions of Asn614 in GluN2A with alanine or glutamine reduced the potency of *R*-ketamine more strongly than that of *S*-ketamine (Extended Data Fig. 5g, h), indicating that Asn614 in GluN2A probably contributed to the binding of *R*-ketamine but not *S*-ketamine. As also observed in MD simulations, Asn614 from one protomer of GluN2A moved towards *R*-ketamine gradually during the simulation, showing a different relative energy contribution from that in the *S*-ketamine system (Extended Data Fig. 5c, f, Extended Data Tables 2, 4). This may provide some clues for explaining the differential binding effects of Asn614 to *S*- and *R*-ketamine.

In conclusion, we have shown that steric-sensitive hydrophobic (Leu642 of GluN2A and Leu643 of GluN2B) and hydrogen-bond interactions (Asn616 of GluN1) are essential to stabilize the binding of ketamine enantiomers in both di-heteromeric GluN1–GluN2A and GluN1–GluN2B NMDA receptors. We speculate that ketamine also resides in the pouch of GluN1–GluN2A–GluN2B receptors[25], as the key binding residues (Asn616 in GluN1, Leu642 in GluN2A and Leu643 in GluN2B) are all conserved in the tri-heteromeric receptors (Extended Data Fig. 6a, c). This central vestibule also contains binding sites for MK-801 and memantine[20,25] (Extended Data Fig. 6b). In general, all three molecules adopt similar 'inverted triangle' configurations through hydrophobic interactions with the TM3 helix and hydrogen bonds with the QRN site. According to the crystal structure[20] and functional data[23], MK-801 forms extensive contacts with Asn614 and Val642 in *Xenopus* GluN1, and with Asn612, Asn613 and Leu640 in *Xenopus* GluN2B (Extended Data Fig. 6b). Therefore, we speculate this might be the molecular basis for the difference in binding affinity between MK-801 and ketamine.

We also carried out structural comparison to analyse whether the key residues for ketamine binding are conserved among ionotropic glutamate receptors. The homologous sites for Asn616 in GluN1 are glutamine or arginine in GluA2 AMPA (α-amino-3-hydroxy-5-methyl-4-isoxazole propionic acid) and GluK2 kainate receptor subunits (Extended Data Fig. 6a, d, e). The longer side chains of glutamine and arginine are likely to cause steric disruption with ketamine. Our data also demonstrated that GluN1(N616Q)–GluN2A receptors showed a marked reduction in ketamine-mediated inhibition (Fig. 3c). Moreover, the homologous sites for Leu642 in GluN2A are isoleucine on both AMPA and kainate receptors. The presence of isoleucine might weaken this steric-sensitive hydrophobic contact, consistent with the reduced ability of ketamine to inhibit GluN1–GluN2A(L642I) and GluN1–GluN2B(L643I) receptors (Fig. 3d, Extended Data Fig. 4b). The amino acid difference at these two key sites might determine the selectivity of ketamine for NMDA receptors rather than AMPA and kainate receptors.

Studies in rodents have suggested that the ketamine metabolite hydroxynorketamine (HNK) could be an antidepressant candidate that acts through NMDA receptor-independent pathways[26,27]. Our results suggest that the hydroxyl group on cyclohexane in HNK might be able to disrupt the hydrophobic interaction with leucine in GluN2 subunits, making HNK much less potent in blocking NMDA receptors, as previously reported[27]. Thus, the structural basis of ketamine binding to NMDA receptors reported here could facilitate ketamine-based drug development, focusing on ketamine derivatives and metabolites that have desirable interactions with human NMDA receptors.

Online content

Any methods, additional references, Nature Research reporting summaries, source data, extended data, supplementary information, acknowledgements, peer review information; details of author contributions and competing interests; and statements of data and code availability are available at https://doi.org/10.1038/s41586-021-03769-9.

1. Autry, A. E. et al. NMDA receptor blockade at rest triggers rapid behavioural antidepressant responses. *Nature* **475**, 91–95 (2011).
2. Berman, R. M. et al. Antidepressant effects of ketamine in depressed patients. *Biol. Psychiatry* **47**, 351–354 (2000).

3. Fava, M. et al. Double-blind, placebo-controlled, dose-ranging trial of intravenous ketamine as adjunctive therapy in treatment-resistant depression (TRD). *Mol. Psychiatry* **25**, 1592–1603 (2020).
4. Ebert, B., Mikkelsen, S., Thorkildsen, C. & Borgbjerg, F. M. Norketamine, the main metabolite of ketamine, is a non-competitive NMDA receptor antagonist in the rat cortex and spinal cord. *Eur. J. Pharmacol.* **333**, 99–104 (1997).
5. Malhi, G. S. & Mann, J. J. Depression. *Lancet* **392**, 2299–2312 (2018).
6. Trivedi, M. H. et al. Medication augmentation after the failure of SSRIs for depression. *N. Engl. J. Med.* **354**, 1243–1252 (2006).
7. Turner, E. H. Esketamine for treatment-resistant depression: seven concerns about efficacy and FDA approval. *Lancet Psychiatry* **6**, 977–979 (2019).
8. Wilkinson, S. T. et al. The effect of a single dose of intravenous ketamine on suicidal ideation: a systematic review and individual participant data meta-analysis. *Am. J. Psychiatry* **175**, 150–158 (2018).
9. Yang, Y. et al. Ketamine blocks bursting in the lateral habenula to rapidly relieve depression. *Nature* **554**, 317–322 (2018).
10. Duman, R. S., Aghajanian, G. K., Sanacora, G. & Krystal, J. H. Synaptic plasticity and depression: new insights from stress and rapid-acting antidepressants. *Nat. Med.* **22**, 238–249 (2016).
11. Moda-Sava, R. N. et al. Sustained rescue of prefrontal circuit dysfunction by antidepressant-induced spine formation. *Science* **364**, eaat8078 (2019).
12. Paoletti, P., Bellone, C. & Zhou, Q. NMDA receptor subunit diversity: impact on receptor properties, synaptic plasticity and disease. *Nat. Rev. Neurosci.* **14**, 383–400 (2013).
13. Karakas, E. & Furukawa, H. Crystal structure of a heterotetrameric NMDA receptor ion channel. *Science* **344**, 992–997 (2014).
14. Zhu, S. et al. Mechanism of NMDA receptor inhibition and activation. *Cell* **165**, 704–714 (2016).
15. Jalali-Yazdi, F., Chowdhury, S., Yoshioka, C. & Gouaux, E. Mechanisms for zinc and proton inhibition of the GluN1/GluN2A NMDA receptor. *Cell* **175**, 1520–1532.e15 (2018).
16. Chou, T. H., Tajima, N., Romero-Hernandez, A. & Furukawa, H. Structural basis of functional transitions in mammalian NMDA receptors. *Cell* **182**, 357–371.e13 (2020).
17. Jelen, L. A., Young, A. H. & Stone, J. M. Ketamine: a tale of two enantiomers. *J. Psychopharmacol.* **35**, 109–123 (2021).
18. Erreger, K., Dravid, S. M., Banke, T. G., Wyllie, D. J. & Traynelis, S. F. Subunit-specific gating controls rat NR1/NR2A and NR1/NR2B NMDA channel kinetics and synaptic signalling profiles. *J. Physiol.* **563**, 345–358 (2005).
19. Burnashev, N. et al. Control by asparagine residues of calcium permeability and magnesium blockade in the NMDA receptor. *Science* **257**, 1415–1419 (1992).
20. Song, X. et al. Mechanism of NMDA receptor channel block by MK-801 and memantine. *Nature* **556**, 515–519 (2018).
21. Durham, R. J. et al. Conformational spread and dynamics in allostery of NMDA receptors. *Proc. Natl Acad. Sci. USA* **117**, 3839–3847 (2020).
22. Iacobucci, G. J. et al. Cross-subunit interactions that stabilize open states mediate gating in NMDA receptors. *Proc. Natl Acad. Sci. USA* **118**, e2007511118 (2021).
23. Kashiwagi, K. et al. Channel blockers acting at *N*-methyl-D-aspartate receptors: differential effects of mutations in the vestibule and ion channel pore. *Mol. Pharmacol.* **61**, 533–545 (2002).
24. Chang, L. et al. Comparison of antidepressant and side effects in mice after intranasal administration of (*R,S*)-ketamine, (*R*)-ketamine, and (*S*)-ketamine. *Pharmacol. Biochem. Behav.* **181**, 53–59 (2019).
25. Lü, W., Du, J., Goehring, A. & Gouaux, E. Cryo-EM structures of the triheteromeric NMDA receptor and its allosteric modulation. *Science* **355**, eaal3729 (2017).
26. Zanos, P. et al. NMDAR inhibition-independent antidepressant actions of ketamine metabolites. *Nature* **533**, 481–486 (2016).
27. Lumsden, E. W. et al. Antidepressant-relevant concentrations of the ketamine metabolite (2*R*,6*R*)-hydroxynorketamine do not block NMDA receptor function. *Proc. Natl Acad. Sci. USA* **116**, 5160–5169 (2019).

Article

Methods

Plasmid construction

The constructs used for cryo-EM studies were wild-type (WT) human GluN1-1a (residues 1–847, GenBank: NP_015566), GluN2A (residues 1–841, GenBank: NP_000824) and GluN2B (residues 1–842, GenBank: NP_000825), cloned into the bicistronic pEG-BacMam vector. For the GluN1–GluN2A receptor, a 3C protease cleavage site, an enhanced GFP and an affinity tag (6×His for GluN1 and Strep II for GluN2A) were placed at the C terminus, and a peptide fragment of the GluA2(Y837–K847) AMPA receptor was inserted after the M4 helix in GluN2A to improve the expression level and thermostability[28,29]. For the GluN1–GluN2B receptor, a 3C protease site and a Strep II tag were ligated before the stop codon of the GluN2B subunit. For electrophysiology, full-length human GluN1-1a and GluN2 or C-terminal truncated constructs were cloned into pcDNA3-based vectors. Site-directed mutagenesis was performed on the WT plasmid using Takara KOD-F_X DNA polymerase.

Protein expression and purification

Recombinant baculovirus with bicistronic vector containing both GluN1 and GluN2A (GluN2B) was produced using sf9 insect cells according the instructions for the Bac-to-Bac TOPO Expression System (Invitrogen A11339). Suspended HEK293S GnTI⁻ cells at 3.0×10^6 cells/ml were infected with P2 virus encoding GluN1 and GluN2 subunits at a molar ratio of 1:1. Twelve hours after infection, 100 μM memantine was added to the cells to avoid NMDA receptor-mediated excitotoxicity, and 10 mM sodium butyrate was added to enhance protein expression. Cells were collected 60 h after infection. To completely remove memantine contamination, membrane fractions were extracted and further dialysed in TBS buffer (150 mM NaCl, 20 mM Tris, pH 8.0) plus 1 mM glycine and 1 mM glutamate for 3–4 days. Afterwards, the membrane was solubilized in TBS containing 1% lauryl maltose neopentyl glycol (L-MNG), 2 mM cholesterol hemisuccinate (CHS), a protease inhibitor cocktail of 0.8 μM aprotinin, 2 mM pepstatin A, 2 μg/ml leupeptin and 1 mM phenylmethyl sulfonyl fluoride (PMSF), 1 mM glycine and 1 mM glutamate for 1.5 h. After ultracentrifugation at 40,000 rpm, the supernatant was purified using Strep-tactin resin, and the protein was eluted with TBS buffer supplemented with 0.1% L-MNG, 2 mM CHS, 5 mM D-desthiobiotin. To remove the fused GFP, GluN1–GluN2A receptor protein was further digested with 3C protease (1:20 molar ratio) overnight. Digested GluN1–GluN2A receptor or eluted GluN1–GluN2B receptor protein was injected into a Superose 6 Increase column (GE Healthcare) for size-exclusion chromatography (SEC) in TBS buffer supplemented with 0.1% digitonin, 5 μM CHS, 0.1 mM CHAPSO, 1 mM glycine, 1 mM glutamate and 50 μM ethylenediamine tetraacetic acid (EDTA), pH adjusted to 8.0. The peak fraction was concentrated to 4–5 mg/ml. All purification procedures were conducted at 4 °C. In addition, we verified that there was no detectable amount of memantine in the protein sample by high-performance liquid chromatography.

Sample preparation and data collection

A 2.5-μl NMDA receptor sample supplemented with 5 mM S-ketamine was applied to a glow-discharged Quantifoil grid 1.2/1.3 Au mesh grid, and then blotted and plunge-frozen in liquid ethane using an FEI Vitrobot in a chamber with 100% humidity at 8 °C. Both datasets were collected on a Titan Krios cryo-electron microscope operating at 300 kV using a K3 in super-resolution mode and then 2 × 2 binned in Fourier space. The images were recorded with a calibrated pixel size of 0.830 Å for GluN1–GluN2A and 0.856 Å for GluN1–GluN2B receptors, at nominal focus values from −1.5 to −3.0 μm, at a total dose of 60 e⁻/Å² with 40 frames and with an energy filter (Gatan). Automatic data collection was conducted using Serial EM or FEI EPU.

Cryo-EM image analysis

The super-resolution counting images were motion corrected and dose-weighted by MotionCor2[30]. Defocus values were estimated using Gctf[31]. Approximately 1,500 particles were manually picked and subjected to an initial reference-free 2D classification. Six to eight representative 2D class averages were selected as templates for autopicking as implemented in the Relion 3.1 workflow[32]. The autopicked particles were subjected to several rounds of 2D classification to remove 'junk' particles. The particles in good 2D-average classes were selected for 3D classification without imposing symmetry using previous structures as reference models (PDB 6IRA for GluN1–GluN2A[29] and PDB 6WHT for GluN1–GluN2B[16]) and low-pass filtered to 50 Å. The 3D classes were inspected using UCSF Chimera[33]. Uninterpretable, low-population, or poorly defined classes were discarded. The 3D classes with similar conformations were then combined and processed for auto refinement. Final density maps were obtained after rounds of CTF refinement and Bayesian polishing. The 'gold-standard' FSC resolution plots were calculated with a soft shape mask applied to independent unfiltered half maps. More information concerning data collection and analysis can be found in Extended Data Fig. 2 and Extended Data Table 1.

Model building

The model of GluN1–GluN2A (PDB 6IRA) or GluN1–GluN2B receptor (PDB 6WHT) was divided into individual lobes of NTD, LBD and TMD using Pymol 2.1.1, and docked into our cryo-EM density maps using Chimera[33]. The PDB coordinates of human GluN1–GluN2A and GluN1–GluN2B receptors were manually inspected and corrected to fit into the density using Coot 0.8.9. Both structures were further processed according to the density maps using Phenix real space refinement[34] with secondary structure and Ramachandran restraints.

Electrophysiology

We injected 0.5–1.0 ng of cDNAs or cRNAs encoding wild-type or mutant GluN1-1a and GluN2A (or GluN2B) into Xenopus laevis at a ratio of 1:1. TEVC recording was performed 12–48 h after injection in extracellular solution containing 100 mM NaCl, 0.3 mM $BaCl_2$, 2.5 mM KCl, 10 μM DTPA and 5 mM HEPES, at pH 7.3. Maximal response currents were evoked by saturating glycine and glutamate (100 μM each).

Unless R-ketamine or S-ketamine was specified, an (R,S)-ketamine racemic mixture was used throughout the TEVC experiments. Ketamine dose–response curves (DRCs) were generated by the simultaneous application of different concentrations of ketamine supplied with 100 μM glycine and 100 μM glutamate, at a holding potential of −60 mV. Data were collected using pClamp 10 (Molecular Devices) and Clampex 10.6, analysed using Clampfit 10.6 and fitted in GraphPad Prism. DRCs were fitted with the following Hill equation: response = $1/[1 + (IC_{50}/concentration)^H]$, in which H is the Hill slope. The magnesium current–voltage (I–V) ramp was performed at voltages ranging from −100 mV to +60 mV in steps of 20 mV by 2-s ramps at 100 μM $MgCl_2$. For I–V curve presentation, after subtraction of the background leak current, the current response and corresponding voltage values were plotted as a line chart in a coordinate frame.

Molecular docking

As the 3D structure of R-ketamine in complex with GluN1–GluN2A has not been determined, flexible molecular docking was carried out to predict the complex structure. The cryo-EM structure of the GluN1–GluN2A TMD was selected as the receptor and the structure of R-ketamine downloaded from the PubChem database was used as the ligand. First, the ligand structure was optimized using Chem3D Pro14.0 and prepared by AutoDockTools software[35] including addition of hydrogens, computation of Gasteiger charges and assignment of rotatable bonds. Then, after the ligand was removed from the complex,

the receptor structure was prepared using AutoDockTools, and residues that interacted with *S*-ketamine were assigned as flexible amino acids. Afterwards, molecular docking was performed using AutoDock 4.0[35]. During the docking procedure, a 3D potential grid was created by the AutoGrid algorithm. The dimensions of the calculated grid maps were $60 \times 60 \times 60$ points with a spacing of 0.375 Å. The docking parameters of genetic algorithm (GA) were set to the default values. Finally, the docked *R*-ketamine−TMD complex of the GluN1−GluN2A receptor was selected according to the position of *R*-ketamine, which is in the central vestibule.

MD simulation

For the *S*-ketamine system, the cryo-EM structure of the GluN1−GluN2A TMD in complex with *S*-ketamine was selected as the initial structure. The missing residues from R582 to T602 in GluN1 and Y578 to F599 in GluN2A (M1−M2 loop) were added by Modeller 9.24[36]. AutoModel and LoopModel class of Modeller were applied to generated missing loops based on the cryo-EM structure of TMD in GluN1−GluN2A. After evaluation of generated models with the lowest value of DOPE scores, the most suitable model was further validated by Ramachandran plot, which showed that 94.34% residues were located in the preferred region. Then, the structure was refined by the Protein Preparation Wizard Workflow integrated in Maestro[37] and all the parameters were set to the default values. The protonation states of all titratable residues as well as the ligand were assigned with PROPKA, at pH 7.0. Under these conditions, the secondary amine of *S*-ketamine was protonated, and the overall charge of the ligand was +1. The CGenFF program[38] was used to assign atomic charges and atom types to *S*-ketamine in the CHARMM General Force Field. Afterwards, the refined structure was embedded in a pre-equilibrated palmitoyloleoylphosphatidylcholine (POPC) bilayer containing 304 lipid molecules by orienting the TMD properly in the membrane using CHARMM-GUI[39]. The generated system was solvated by TIP3P waters and neutralized with 0.2 M NaCl, leading to a total of 146,680 atoms. For the *R*-ketamine system, the complex structure of *R*-ketamine−GluN1−GluN2A-TMD predicted by molecular docking was used as the initial structure, and the other steps were similar to those for the *S*-ketamine system, leading to a total of 145,549 atoms.

The MD simulations were performed with the Gromacs 2019.6 program package using CHARMM36 all-atom force field. First, the solvated system was subjected to energy minimization using the steepest descent algorithm, with a series of restraints for the protein, ligand and lipid atoms. Subsequently, the minimized systems were heated from 0 to 310 K, and then equilibrated at constant pressure and temperature (NPT ensemble; 310 K, 1 bar) by gradually decreasing the positional restraints on the protein, ligand and lipid atoms. The parameter files of the MD simulation were obtained from the CHARMM-GUI website. The results of the MD simulations were analysed by Gromacs tools and VMD.

Per-residue decomposition studies of relative binding energy

The energy contributions of residues within 10 Å of *S*-ketamine were observed based on the relative binding energy ($\Delta G_{binding}$) calculation by the MM-PBSA approach using g_mmpbsa, which does not include the contribution of entropic terms and calculates only the enthalpic component of the binding energy[40]. On the basis of the equilibrated dynamic trajectories of the *S*-ketamine system, a total of 100 snapshots were taken from the last 10-ns trajectory with an interval of 100 ps. The calculations of electrostatic energy, van der Waals energy and polar solvation energy were performed by the Poisson−Boltzmann solver (APBS) method, while the nonpolar energy was calculated using the solvent-accessible surface area (SASA) method. Furthermore, the Python scripts 'MmPbSaStat.py' and 'MmPbSaDecomp.py' were used for the MM-PBSA calculations and individual contributions of different amino acids. The grid spacing and probe radius were set to 0.5 Å and 1.4 Å, respectively, for SASA approximation. The solvent dielectric constant was set to 80, and the solute dielectric constant was set to 2.

Ligand-binding assay

Cell pellets of GluN1−GluN2A$_{EM}$ and GluN1−GluN2B$_{EM}$ receptors, and cortex from adult rats, were collected, resuspended with 50 mM Tris-HCl (pH 7.4), homogenized and ultracentrifuged. Membrane fractions were washed several times and suspended in assay buffer (50 mM Tris-HCl, 1 mM glycine and 1 mM glutamate, pH 7.4). The binding assays were set up in 96-well plates using [^{3}H]MK-801 (10 nM for GluN1−GluN2A$_{EM}$ receptor and rat cortex; 50 nM for GluN1−GluN2B$_{EM}$ receptor) and membranes (100 µg per well) in a final volume of 100 µl per well in assay buffer. *S*-ketamine was distributed in 96-well plates (starting at 500 µM, eight-point fourfold serial dilution) in triplicate and shaken at 300 rpm for 1 h. The reactions were harvested with a Unifilter-96 GF/C filter plate pre-soaked with 0.3% polyethyleneimine using PerkinElmer Filtermate Harvester, followed by four washes with chilled wash buffer (50 mM Tris HCl, pH 7.4). Filters were microwave-dried and Perkin Elmer Microscint 20 cocktail was added. The radioactivity retained on the filters was counted using a Perkin Elmer MicroBeta2 Reader. The data were analysed with GraphPad Prism 5.0.

Drugs and chemicals

The racemic ketamine, *S*-ketamine and *R*-ketamine used in this paper were provided by the drug reference materials laboratory of the Third Research Institute of Ministry of Public Security. Contact email: phtnwfat@163.com.

Reporting summary

Further information on research design is available in the Nature Research Reporting Summary linked to this paper.

Data availability

The cryo-EM maps and structure coordinates for GluN1−GluN2A and GluN1−GluN2B receptors have been deposited in the Electron Microscopy Data Bank under accession numbers EMD-31308 and EMD-31309, and in the Protein Data Bank under accession numbers 7EU7 and 7EU8, respectively. The structures of *S*-ketamine and *R*-ketamine are accessible from the PubChem database (https://pubchem.ncbi.nlm.nih.gov/) under compound CIDs 182137 and 644025, respectively. The human missense mutation c.1925T>G (L642R) in *GRIN2A* was retrieved from the ClinVar database (https://www.ncbi.nlm.nih.gov/clinvar/) under variation ID 985631. Additional data that support the findings of this study are available from the corresponding author upon request.

28. Lee, C. H. et al. NMDA receptor structures reveal subunit arrangement and pore architecture. *Nature* **511**, 191–197 (2014).
29. Zhang, J. B. et al. Structural basis of the proton sensitivity of human GluN1-GluN2A NMDA receptors. *Cell Rep.* **25**, 3582–3590.e4 (2018).
30. Zheng, S. Q. et al. MotionCor2: anisotropic correction of beam-induced motion for improved cryo-electron microscopy. *Nat. Methods* **14**, 331–332 (2017).
31. Zhang, K. Gctf: real-time CTF determination and correction. *J. Struct. Biol.* **193**, 1–12 (2016).
32. Zivanov, J., Nakane, T. & Scheres, S. H. W. Estimation of high-order aberrations and anisotropic magnification from cryo-EM data sets in *RELION*-3.1. *IUCrJ* **7**, 253–267 (2020).
33. Pettersen, E. F. et al. UCSF Chimera—a visualization system for exploratory research and analysis. *J. Comput. Chem.* **25**, 1605–1612 (2004).
34. Adams, P. D. et al. PHENIX: a comprehensive Python-based system for macromolecular structure solution. *Acta Crystallogr. D* **66**, 213–221 (2010).
35. Morris, G. M. et al. AutoDock4 and AutoDockTools4: automated docking with selective receptor flexibility. *J. Comput. Chem.* **30**, 2785–2791 (2009).
36. Webb, B. & Sali, A. Comparative protein structure modeling using MODELLER. *Curr. Protoc. Bioinformatics* **54**, 5.6.1–5.6.37 (2016).
37. Schrodinger, LLC *Maestro, Version 9.0* (2009).
38. Vanommeslaeghe, K. & MacKerell, A. D., Jr. Automation of the CHARMM General Force Field (CGenFF) I: bond perception and atom typing. *J. Chem. Inf. Model.* **52**, 3144–3154 (2012).
39. Jo, S., Kim, T., Iyer, V. G. & Im, W. CHARMM-GUI: a web-based graphical user interface for CHARMM. *J. Comput. Chem.* **29**, 1859–1865 (2008).
40. Kumari, R., Kumar, R., Open Source Drug Discovery Consortium & Lynn, A. g_mmpbsa—a GROMACS tool for high-throughput MM-PBSA calculations. *J. Chem. Inf. Model.* **54**, 1951–1962 (2014).

Article

41. Chen, S. et al. Activation and desensitization mechanism of AMPA receptor-TARP complex by cryo-EM. *Cell* **170**, 1234–1246.e14 (2017).
42. Meyerson, J. R. et al. Structural basis of kainate subtype glutamate receptor desensitization. *Nature* **537**, 567–571 (2016).

Author contributions Y.Z. and T.Z. purified and froze the protein, collected and analysed the cryo-EM data, built the atomic model and conducted electrophysiology on GluN1–GluN2A and GluN1–GluN2B receptors, respectively; F.Y., L.Z., and C.L. carried out the docking and MD simulation; D.D. assisted with binding assays; S.L. and F.G. participated in the data analysis; H.L. provided ketamine compounds; Y.Z., F.Y., T.Z. and S.Z wrote the manuscript with inputs from all the authors. S.Z. conceived the project and supervised the research.

Competing interests The authors declare no competing interests.

Additional information
Supplementary information The online version contains supplementary material available at https://doi.org/10.1038/s41586-021-03769-9.
Correspondence and requests for materials should be addressed to C.L. or S.Z.
Peer review information *Nature* thanks the anonymous reviewers for their contribution to the peer review of this work. Peer reviewer reports are available.
Reprints and permissions information is available at http://www.nature.com/reprints.
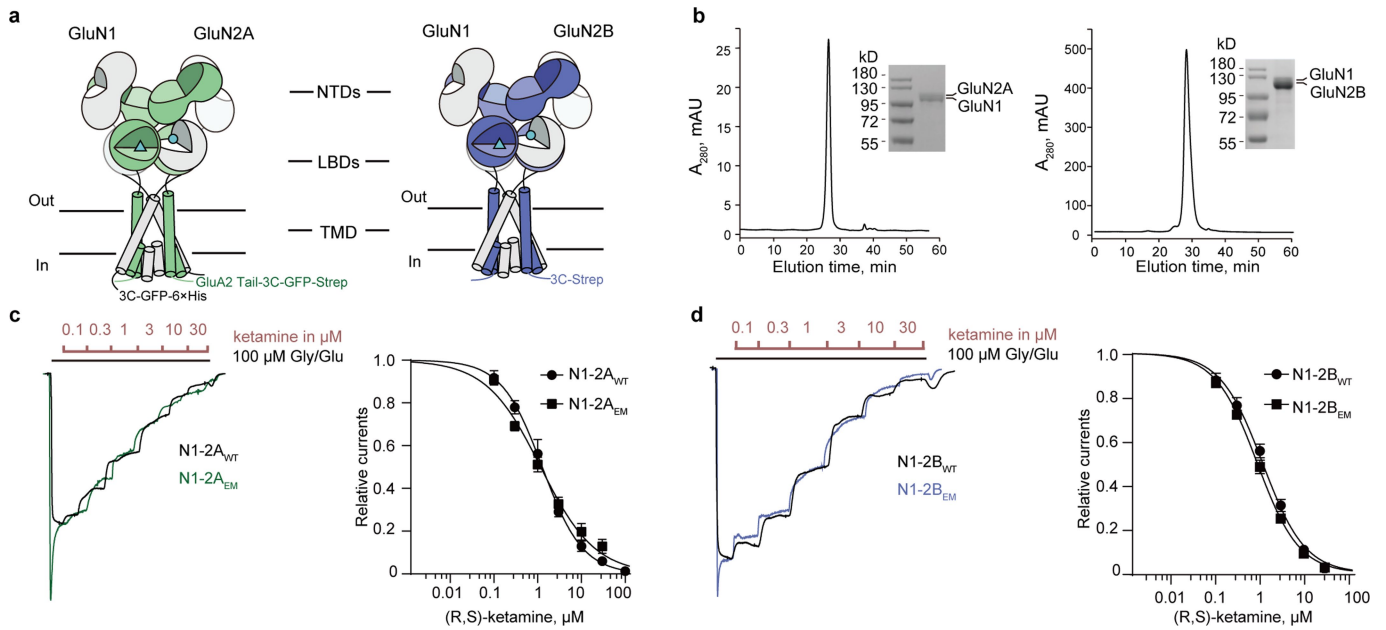
Extended Data Fig. 1 | Expression profile and functional validation of human GluN1–GluN2A and GluN1–GluN2B NMDA receptors. a, Schematic representation of human GluN1$_{EM}$ (grey), GluN2A$_{EM}$ (green) and GluN2B$_{EM}$ (blue) CTD-truncated constructs. **b,** Representative fluorescence SEC and Coomassie blue gel staining of the purified GluN1–GluN2A$_{EM}$ (left) and GluN1–GluN2B$_{EM}$ receptors (right). Experiments were performed three times independently with similar results. **c, d,** Representative recording traces (left) and the fitted DRCs (right; mean ± s.d.) for (R,S)-ketamine inhibition on wild-type GluN1–GluN2A and GluN1–GluN2A$_{EM}$ (**c**), and wild-type GluN1–GluN2B and GluN1–GluN2B$_{EM}$ (**d**) receptors activated with 100 μM coagonists. Ketamine IC$_{50}$ values, Hill slopes and numbers are listed in Extended Data Table 3.
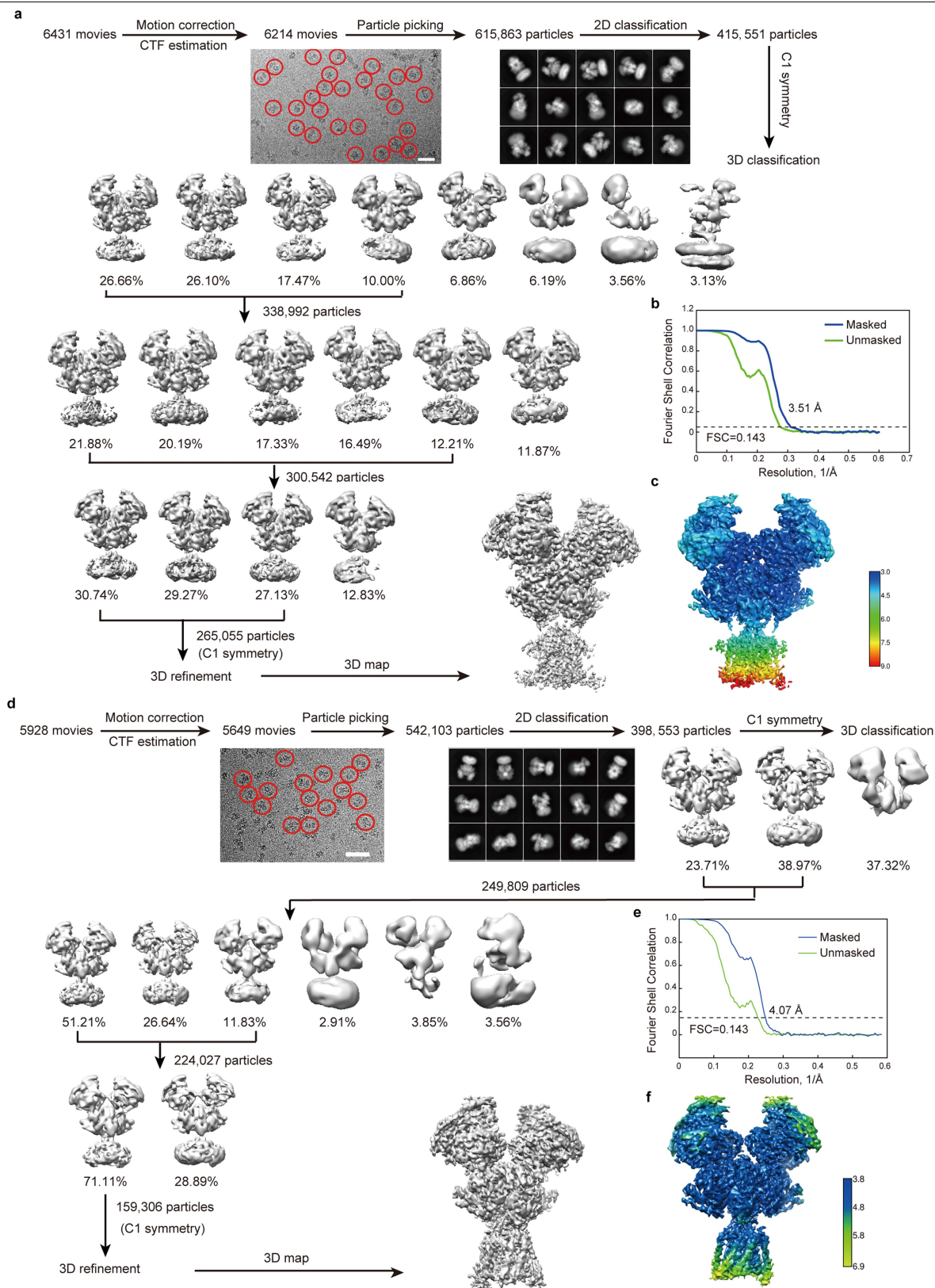
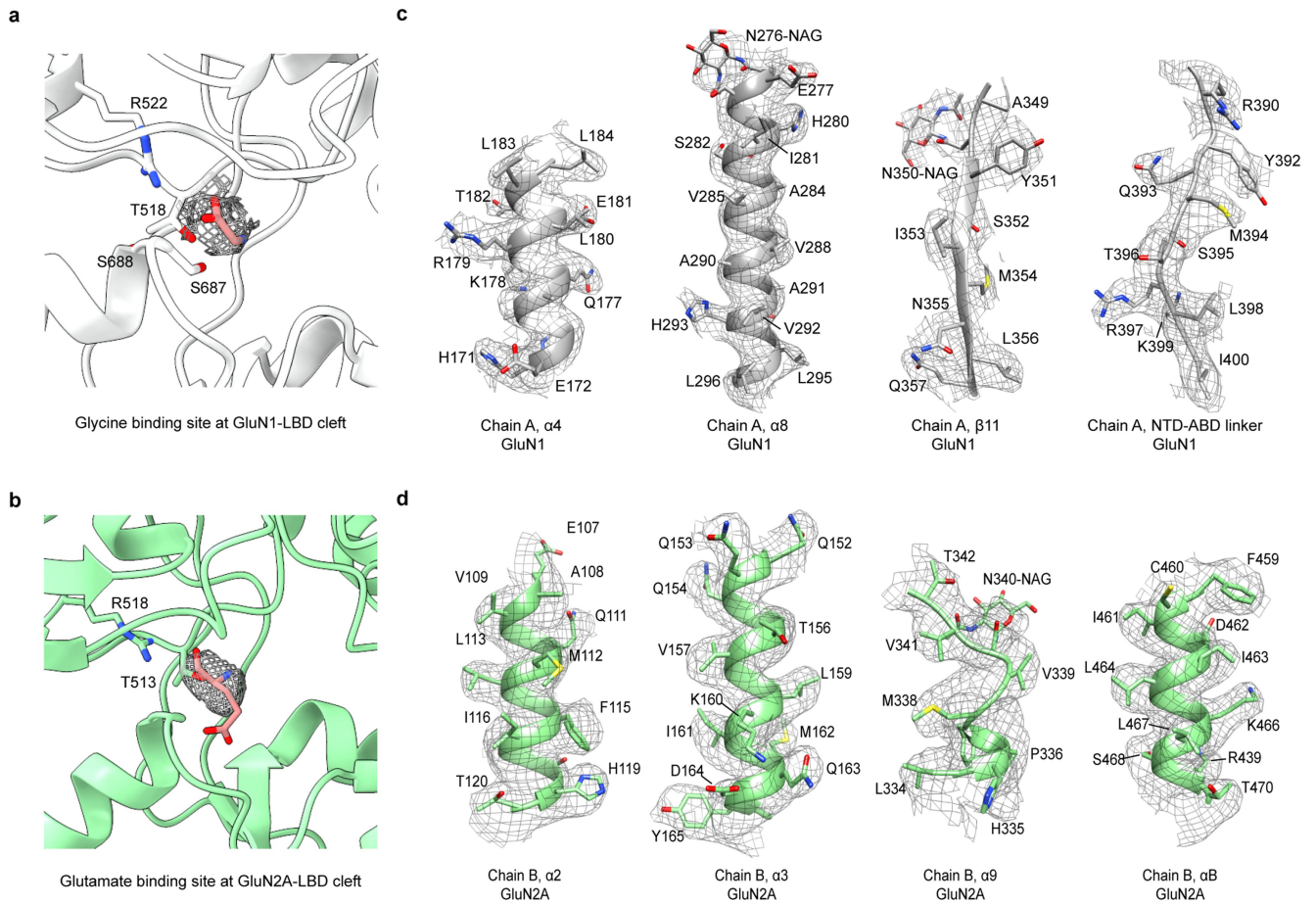**Extended Data Fig. 2 | Overview of cryo-EM image processing and 3D reconstruction of GluN1–GluN2A and GluN1–GluN2B NMDA receptors. a**, Flowchart of the image processing and 3D reconstruction of human GluN1– GluN2A receptors in complex with *S*-ketamine, glycine and glutamate. Typical single particles are circled in red from raw micrographs. The 2D class average images show characteristic 2D views in various orientations. The 3D classes with similar conformations were selected and combined through several rounds of 3D classification for final refinement. **b**, Fourier shell correlation (FSC) curve for the resolution estimation. **c**, Side view of the cryo-EM density map of GluN1–GluN2A receptor coloured by local resolution estimated by Relion 3.1. **d**, Pipelines for single-particle analysis and reconstruction of human GluN1– GluN2B receptor in complex with *S*-ketamine, glycine and glutamate. Same workflow as in **a**. **e**, FSC curve for the resolution estimation. **f**, Side view of the cryo-EM density map of GluN1–GluN2B receptor coloured by local resolution estimated by Relion 3.1.

a

Glycine binding site at GluN1-LBD cleft

b

Glutamate binding site at GluN2A-LBD cleft

c

Chain A, α4
GluN1

Chain A, α8
GluN1

Chain A, β11
GluN1

Chain A, NTD-ABD linker
GluN1

d

Chain B, α2
GluN2A

Chain B, α3
GluN2A

Chain B, α9
GluN2A

Chain B, αB
GluN2A

Extended Data Fig. 3 | Representative local densities in GluN1–GluN2A cryo-EM map with fitted atomic model. a, **b**, Zoomed-in views of the GluN1-LBD cleft with EM density for glycine (**a**), and the GluN2A-LBD cleft with glutamate (**b**). Key binding residues are shown as sticks. **c**, **d**, Local densities in extracellular domains of the GluN1 (**a**) and GluN2A (**b**) subunits. EM densities are shown as light grey mesh, while the side chains and N-glycosylation sites of residues are represented as sticks.
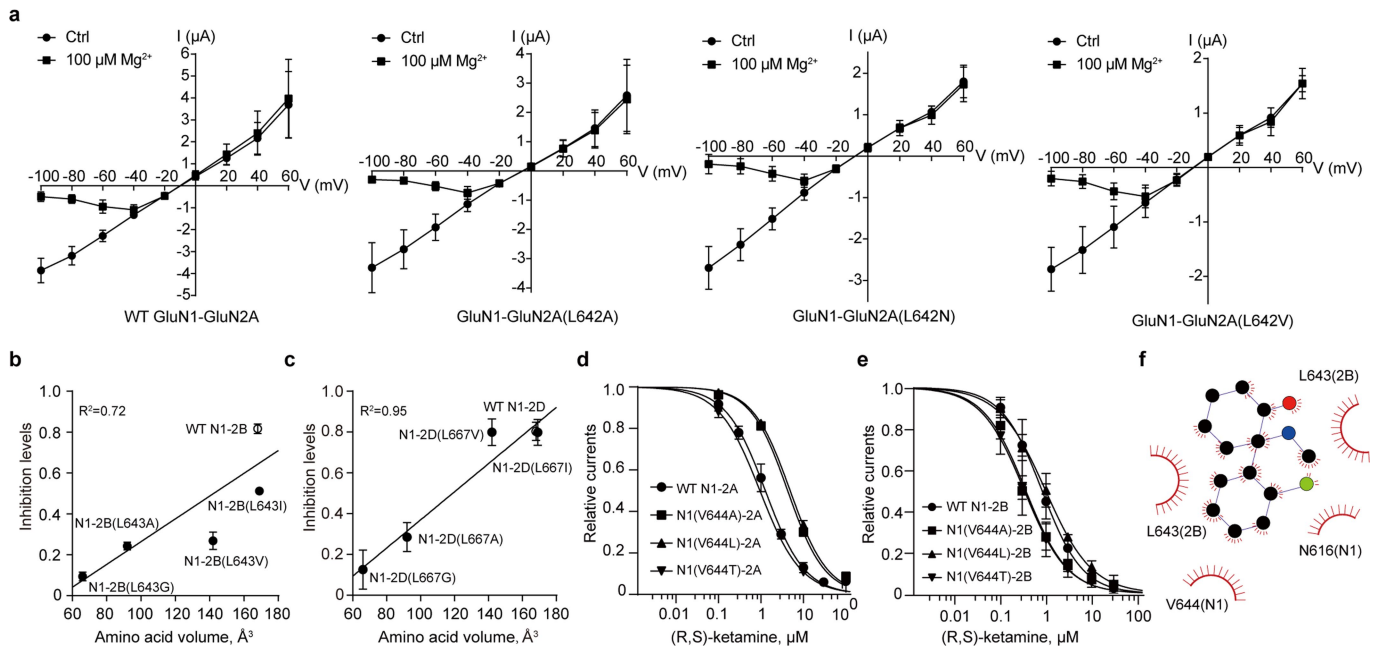
Extended Data Fig. 4 | Functional validation of the ketamine-binding pocket of NMDA receptors. a, Representative $I–V$ curves for Mg^{2+} blockage of wild-type GluN1–GluN2A receptors or receptors incorporating a substitution (A, N or V) at GluN2A-L642, recorded in the presence of 100 μM $MgCl_2$. **b, c,** Plot of 3 μM ketamine inhibition level for wild-type (open circle) and mutant (filled circles) amino acid volume (I, V, A or G) at position GluN2B-L643 or GluN2D-L667, shown with a linear regression. R^2 values equal to 0.72 for GluN1–GluN2B and 0.95 for GluN1–GluN2D receptors. **d, e,** (R,S)-Ketamine DRCs for the GluN1–GluN2A and GluN1–GluN2B wild-type or mutant receptors incorporating a substitution (A, L or T) at GluN1-V644. All IC_{50} values, Hill slopes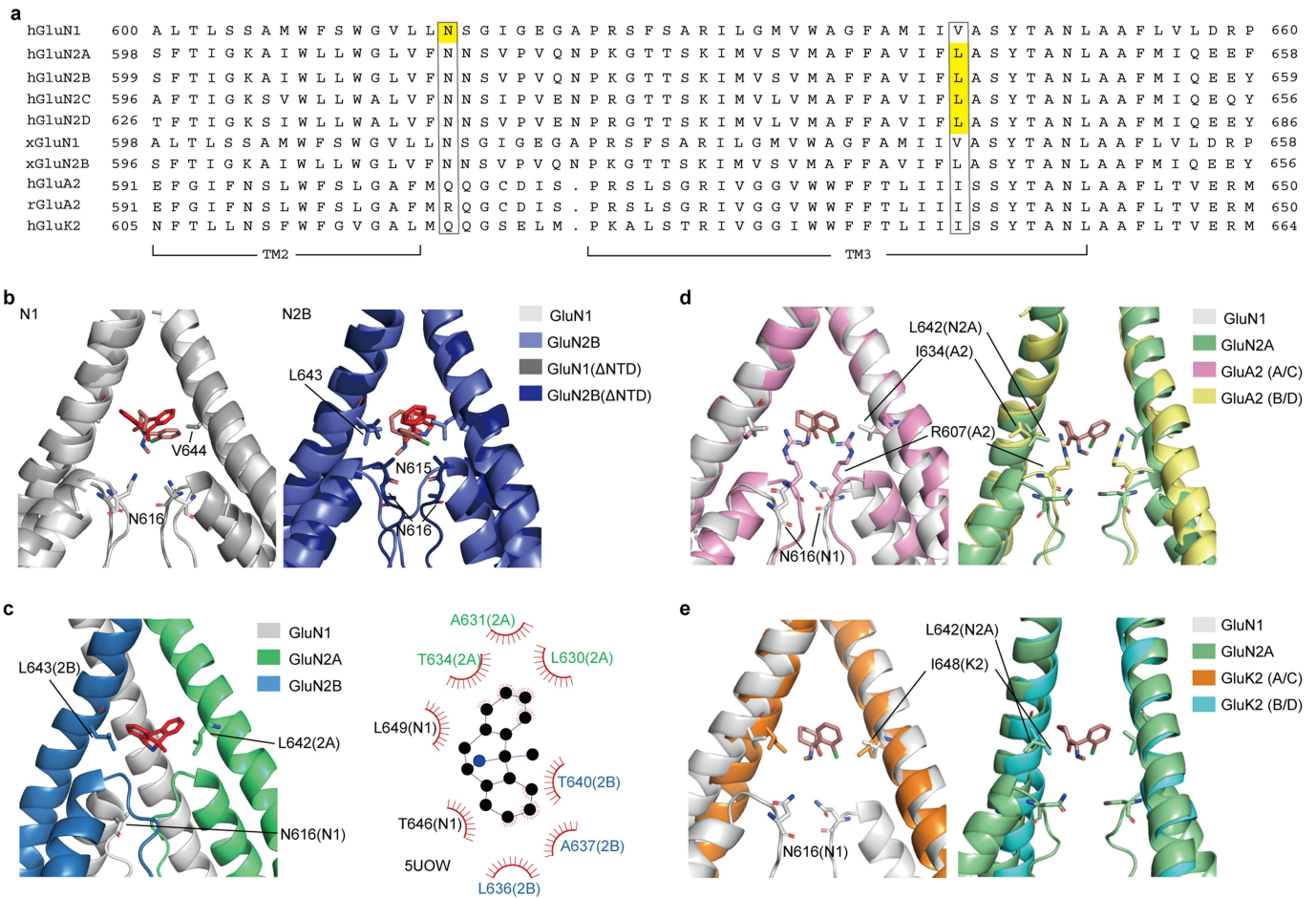 and numbers of oocytes are listed in Extended Data Table 3. **f,** Schematic representation of the S-ketamine binding site on GluN1–GluN2B receptors analysed by Ligplot[+].
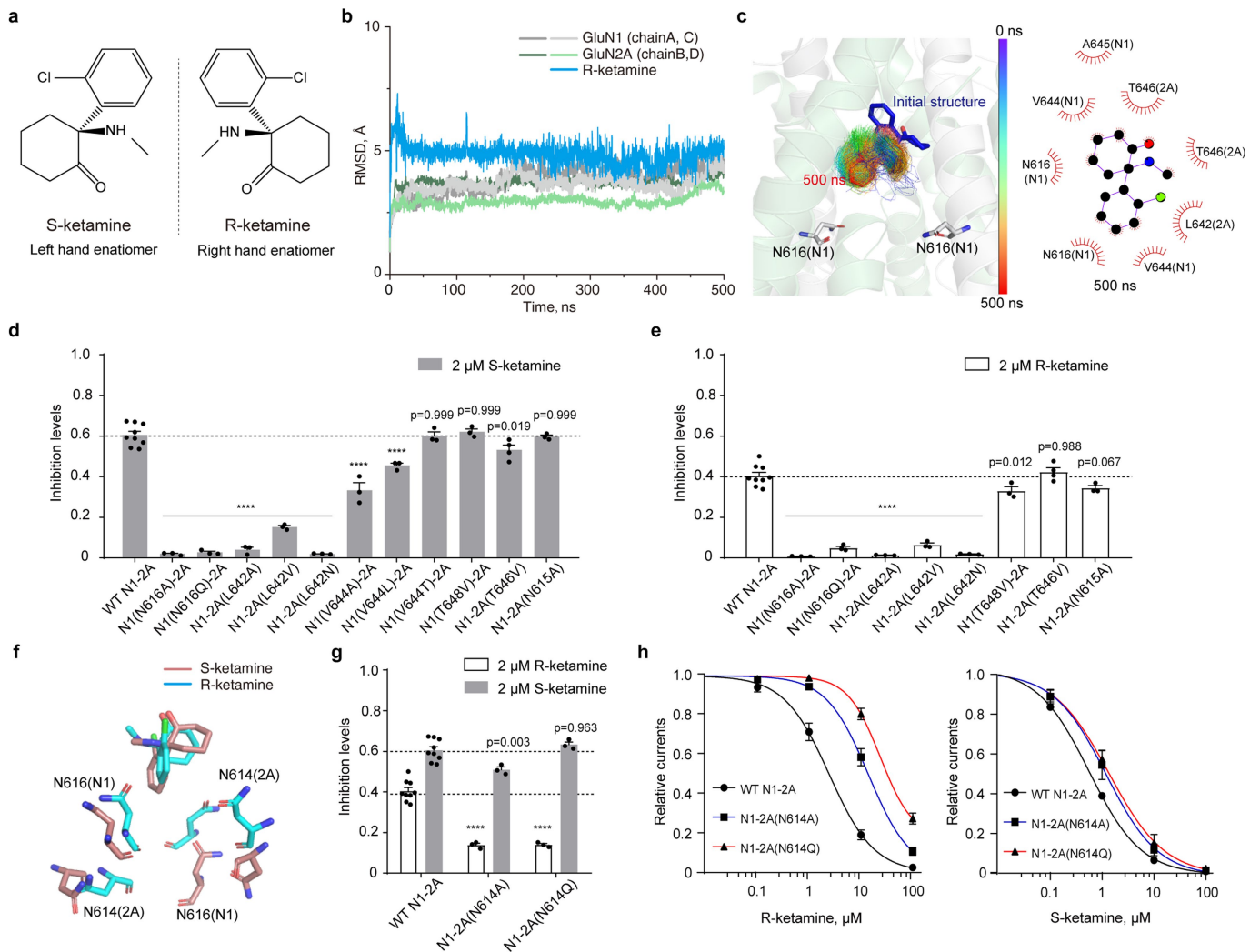
Extended Data Fig. 5 | Molecular basis of *S*- and *R*-ketamine-induced inhibition of GluN1–GluN2A receptors. a, Chemical structures of left-handed *S*-ketamine and right-handed *R*-ketamine. **b**, r.m.s.d. trajectories for each chain (excluding M1–M2 loops) and *R*-ketamine were calculated on Cα atoms based on the initial structure within the whole simulation time of 500 ns. **c**, Left, *R*-ketamine poses obtained in MD simulation along the whole simulation time. Right, schematic diagram of *R*-ketamine and TMD interactions at 500 ns snapshot extracted from MD simulation. Residues involved in the hydrophobic interactions are shown as starbursts. **d**, Inhibition by 2 μM *S*-ketamine of NMDA receptor activity induced by saturating agonists in wild-type GluN1–GluN2A (0.606 ± 0.018, *n* = 9 oocytes), GluN1(N616A)–GluN2A (0.020 ± 0.004, *n* = 3), GluN1(N616Q)–GluN2A (0.027 ± 0.006, *n* = 3), GluN1–GluN2A(L642A) (0.041 ± 0.012, *n* = 3), GluN1–GluN2A(L642V) (0.152 ± 0.007, *n* = 3), GluN1–GluN2A(L642N) (0.020 ± 0.001, *n* = 3), GluN1(V644A)–GluN2A (0.333 ± 0.038, *n* = 3), GluN1(V644L)–GluN2A (0.455 ± 0.012, *n* = 3), GluN1(V644T)–GluN2A (0.602 ± 0.020, *n* = 3), GluN1(T648V)–GluN2A (0.621 ± 0.015, *n* = 3), GluN1–GluN2A(T646V) (0.532 ± 0.024, *n* = 4) and GluN1–GluN2A(N615A)

(0.597 ± 0.008, *n* = 3) receptors. **e**, Inhibition by 2 μM *R*-ketamine of wild-type GluN1–GluN2A (0.404 ± 0.017, *n* = 9), GluN1(N616A)–GluN2A (0.008 ± 0.001, *n* = 3), GluN1(N616Q)–GluN2A (0.049 ± 0.008, *n* = 3), GluN1–GluN2A(L642A) (0.014 ± 0.001, *n* = 3), GluN1–GluN2A(L642V) (0.065 ± 0.009, *n* = 3), GluN1–GluN2A(L642N) (0.019 ± 0.001, *n* = 3), GluN1(T648V)–GluN2A (0.330 ± 0.021, *n* = 3), GluN1–GluN2A(T646V) (0.423 ± 0.021, *n* = 4) and GluN1–GluN2A(N615A) (0.344 ± 0.01, *n* = 3) receptors. **f**, Superposition of the 500 ns snapshots extracted from MD simulation of *S*-ketamine (pink) and *R*-ketamine (cyan) systems, respectively. **g**, Inhibition by 2 μM *R*- and *S*-ketamine of GluN1–GluN2A(N614A) (0.138 ± 0.009, 0.509 ± 0.014, *n* = 3) and GluN1–GluN2A(N614Q) (0.140 ± 0.006, 0.633 ± 0.014, *n* = 3) receptors. In **d**, **e**, **g**, all data shown are mean ± s.e.m.; *P* values are determined by one-way ANOVA with Dunnett's multiple comparison test (****$P < 0.0001$). Each data point represents the result of one oocyte. **h**, *R*-ketamine (left) and *S*-ketamine (right) DRCs (mean ± s.d.) for wild-type GluN1–GluN2A (IC$_{50}$: 2.39 ± 0.45 μM, *n* = 4 oocytes; 0.60 ± 0.03 μM, *n* = 3), GluN1–GluN2A(N614A) (13.66 ± 2.49 μM, *n* = 4; 1.22 ± 0.44 μM, *n* = 4) and GluN1–GluN2A(N614Q) (39.94 ± 6.72 μM, *n* = 4; 1.41 ± 0.38 μM, *n* = 4) receptors.

a, Sequence alignment of TM2–TM3 segments in human GluN1, GluN2A, GluN2B, GluN2C, GluN2D, GluA2 and GluK2, *Xenopus* GluN1, GluN2B and rat GluA2 subunits.

Extended Data Fig. 6 | Sequence alignment and structural comparison of TMD in ionotropic GluRs. a, Sequence alignment of TM2–TM3 segments in human GluN1, GluN2A, GluN2B, GluN2C, GluN2D, GluA2 and GluK2, *Xenopus* GluN1, GluN2B and rat GluA2 subunits. The critical residues involved in ketamine binding are highlighted in yellow, and their homologous sites in ionotropic GluRs are marked in rectangles. **b**, Superposition of the TM2 and TM3 segments between the *S*-ketamine (in brick red)-bound GluN1–GluN2B_EM receptor and the MK-801 (in red)-bound GluN1–GluN2B(ΔNTD)

receptor (PDB code: 5UN1)[20]. **c**, MK-801-bound TMD of the triheteromeric GluN1–GluN2A–GluN2B NMDA receptor, viewed parallel to the membrane (PDB code: 5UOW)[25]. MK-801 binding residues were analysed by LigPlot⁺ (right). **d**, **e**, Superposition of the TM2 and TM3 segments between the *S*-ketamine bound GluN1–GluN2A_EM receptor and GluA2 AMPA receptor (PDB code: 5VOT)[41] (**d**) or the GluK2 kainate receptor (PDB code: 5KUF)[42] (**e**). All superpositions are based on the α-carbon atoms of the conserved SYTANL region.

Extended Data Table 1 | Cryo-EM data collection, refinement and validation statistics

	GluN1-GluN2A receptors (EMDB-31308) (PDB 7EU7)	GluN1-GluN2B receptors (EMDB-31309) (PDB 7EU8)
Data collection and processing		
Magnification	105,000	81,000
Voltage (kV)	300	300
Electron exposure (e–/Å²)	60	60
Defocus range (μm)	-1.5 ~ -3.0	-1.5 ~ -3.0
Pixel size (Å)	0.830	0.856
Symmetry imposed	C1	C1
Initial particle images (no.)	615,863	542,103
Final particle images (no.)	265,055	159,306
Map resolution (Å)	3.51	4.07
FSC threshold	0.143	0.143
Map resolution range (Å)	3.2 ~ 9.9	3.8 ~ 6.9
Refinement		
Initial model used (PDB code)	6IRA	6WHT
Model resolution (Å)	3.5	4.1
FSC threshold	0.143	0.143
Model resolution range (Å)		
Map sharpening B factor (Å²)	-50	-120
Model composition		
Non-hydrogen atoms	21,757	18,654
Protein residues	3,134	3,010
Ligands	24	7
B factors (Å²)		
Protein	108.09	55.39
Ligand	118.90	91.31
R.m.s. deviations		
Bond lengths (Å)	0.004	0.002
Bond angles (°)	0.965	0.402
Validation		
MolProbity score	2.43	1.54
Clashscore	16.18	3.01
Poor rotamers (%)	2.99	3.51
Ramachandran plot		
Favored (%)	94.84	97.86
Allowed (%)	5.03	2.00
Disallowed (%)	0.13	0.14

Article

Extended Data Table 2 | Per-residue decomposition of relative binding energy for residues within 10 Å of S-ketamine

Per-residue energy decomposition of GluN1 (kJ/mol)			Per-residue energy decomposition of GluN2A (kJ/mol)		
Residue	Chain A	Chain C	Residue	Chain B	Chain D
L614	-1.37	/	W558	-0.18	/
L615	-0.81	-1.78	L611	-1.19	-1.18
N616	-0.57	-3.67	V612	-2.12	-1.58
S617	/	0.34	F613	-1.90	-1.41
A637	-1.04	/	N614	0.38	1.86
G638	-0.76	/	N615	-0.09	0.85
F639	-0.34	/	S616	-0.07	-0.82
A640	-0.12	-0.54	V617	-0.14	/
M641	-1.90	-1.57	A635	-0.95	-0.78
I642	-0.74	-0.85	F637	-0.64	-0.49
I643	-0.00	0.12	A638	-0.90	-0.76
V644	-3.67	-0.62	V639	-1.09	-2.54
A645	-2.79	-0.13	I640	-0.89	-0.99
S646	0.32	0.29	F641	0.31	-0.29
Y647	0.59	-0.01	L642	-2.28	-4.74
T648	1.92	2.04	A643	-1.57	-3.33
A649	0.07	0.24	S644	0.18	0.09
N650	0.52	/	Y645	0.03	0.36
L651	0.41	0.57	T646	3.78	0.21
A652	0.55	0.52	A647	0.25	-0.07
			N648	0.63	0.73
			L649	0.43	0.60
			A650	0.57	0.59

Extended Data Table 3 | Summary of potency of (*R*,*S*)-ketamine on human GluN1–GluN2A and GluN1–GluN2B receptors

NMDA receptors	IC_{50}, µM	Hill Slope	n
GluN1-GluN2A$_{WT}$	1.33 ± 0.38	-0.94 ± 0.05	15
GluN1-GluN2A$_{EM}$	1.19 ± 0.19	-0.70 ± 0.06	5
GluN1(N616A)-GluN2A	~ 8258	~ -1.14	3
GluN1(N616Q)-GluN2A	55.38 ± 6.98	-1.06 ± 0.02	3
GluN1-GluN2A(L642V)	9.32 ± 0.68	-0.09 ± 0.08	4
GluN1-GluN2A(L642A)	64.96 ± 13.9	-0.91 ± 0.17	5
GluN1-GluN2A(L642I)	4.84 ± 0.69	-0.93 ± 0.06	4
GluN1-GluN2A(L642G)	129.85 ± 29.9	-0.99 ± 0.05	4
GluN1-GluN2A(L642N)	354.2 ± 35.7	-0.64 ± 0.05	4
GluN1(V644A)-GluN2A	4.33 ± 0.43	-0.99 ± 0.01	4
GluN1(V644L)-GluN2A	4.88 ± 0.42	-0.99 ± 0.02	3
GluN1(V644T)-GluN2A	1.10 ± 0.13	-0.91 ± 0.07	5
GluN1-GluN2A(L642R)	908.7 ± 541.2	-0.72 ± 0.38	5
GluN1-GluN2B$_{WT}$	0.85 ± 0.25	-1.02 ± 0.12	10
GluN1-GluN2B$_{EM}$	0.88 ± 0.08	-0.91 ± 0.04	5
GluN1(N616A)-GluN2B	15.49 ± 1.60	-0.79 ± 0.08	4
GluN1-GluN2B(L643A)	13.60 ± 3.50	-0.97 ± 0.10	6
GluN1(V644A)-GluN2B	0.37 ± 0.10	-0.94 ± 0.02	3
GluN1(V644L)-GluN2B	1.12 ± 0.70	-0.87 ± 0.16	4
GluN1(V644T)-GluN2B	0.37 ± 0.17	-0.96 ± 0.02	4

Recorded at a holding potential of −60 mV. Data shown as mean ± s.d.

Article

Extended Data Table 4 | Per-residue decomposition of relative binding energy for residues within 10 Å of *R*-ketamine

Per-residue energy decomposition of GluN1 (kJ/mol)			Per-residue energy decomposition of GluN2A (kJ/mol)		
Residue	Chain A	Chain C	Residue	Chain B	Chain D
G612	-1.13	-0.91	L611	-0.80	/
V613	-0.94	-1.13	V612	-0.80	-2.61
L614	-2.12	-1.24	F613	-0.89	-1.25
L615	-2.10	-0.10	N614	-1.63	1.29
N616	-1.07	-2.63	N615	-0.58	3.00
S617	-1.13	0.24	S616	-0.16	/
G618	/	0.06	A635	-0.58	/
A637	-0.78	1.00	F636	-0.75	/
G638	-0.74	/	F637	-0.55	/
F639	-0.52	/	A638	-0.69	-0.74
A640	-0.84	-0.68	V639	-2.95	-1.93
M641	-2.32	-3.99	I640	-1.14	-0.95
I642	-1.06	-0.86	F641	-0.34	0.29
I643	-0.22	-0.09	L642	-7.07	-0.14
V644	-2.81	-2.72	A643	-2.63	-0.56
A645	-3.20	-0.68	S644	0.01	0.27
S646	0.31	0.40	Y645	-0.17	0.53
Y647	0.36	1.00	T646	1.50	2.59
T648	1.63	3.45	A647	0.08	0.26
A649	0.11	0.31	N648	0.57	0.22
N650	0.48	/	L649	0.55	0.73
L651	0.70	0.58	A650	0.79	0.77
A652	0.70	/			

nature research

Corresponding author(s): Shujia Zhu, Cheng Luo

Last updated by author(s): 2021-6-14

Reporting Summary

Nature Research wishes to improve the reproducibility of the work that we publish. This form provides structure for consistency and transparency in reporting. For further information on Nature Research policies, see our Editorial Policies and the Editorial Policy Checklist.

Statistics

For all statistical analyses, confirm that the following items are present in the figure legend, table legend, main text, or Methods section.

n/a	Confirmed	
☐	☒	The exact sample size (*n*) for each experimental group/condition, given as a discrete number and unit of measurement
☐	☒	A statement on whether measurements were taken from distinct samples or whether the same sample was measured repeatedly
☐	☒	The statistical test(s) used AND whether they are one- or two-sided *Only common tests should be described solely by name; describe more complex techniques in the Methods section.*
☒	☐	A description of all covariates tested
☐	☒	A description of any assumptions or corrections, such as tests of normality and adjustment for multiple comparisons
☐	☒	A full description of the statistical parameters including central tendency (e.g. means) or other basic estimates (e.g. regression coefficient) AND variation (e.g. standard deviation) or associated estimates of uncertainty (e.g. confidence intervals)
☐	☒	For null hypothesis testing, the test statistic (e.g. *F*, *t*, *r*) with confidence intervals, effect sizes, degrees of freedom and *P* value noted *Give P values as exact values whenever suitable.*
☒	☐	For Bayesian analysis, information on the choice of priors and Markov chain Monte Carlo settings
☒	☐	For hierarchical and complex designs, identification of the appropriate level for tests and full reporting of outcomes
☒	☐	Estimates of effect sizes (e.g. Cohen's *d*, Pearson's *r*), indicating how they were calculated

Our web collection on statistics for biologists contains articles on many of the points above.

Software and code

Policy information about availability of computer code

Data collection Clampex 10.6 was used for electrophysiological data collection. Serial EM 3.8 or FEI EPU 2.11 were used for Cryo-EM image collection.

Data analysis Clampfit 10.6, pClamp 10 and GraphPad Prism-8 were used for electrophysiological data analysis. Relion-3.1, MotionCor2 and Gctf -v1.18 were used for Cryo-EM image analysis. Phenix-1.19, Coot 0.8.9, Chimera-1.15 and Pymol-2.1.1 were used for structural model determination, refinement and analysis. AutoDockTools 1.5.6 and Autodock 4.0 were used for molecular docking. Maestro 9.2, CHARMM-GUI (https://www.charmm-gui.org/) and Gromacs 2019.6 program package were used for structure refinement, simulation system construction and molecular dynamics (MD) simulation. The results of MD simulation were analyzed by Gromacs tools (Gromacs 2019.6) and VMD 1.9.3. Program g_mmpbsa was used for per-residue decomposition energy calculation.

For manuscripts utilizing custom algorithms or software that are central to the research but not yet described in published literature, software must be made available to editors and reviewers. We strongly encourage code deposition in a community repository (e.g. GitHub). See the Nature Research guidelines for submitting code & software for further information.

Data

Policy information about availability of data

All manuscripts must include a data availability statement. This statement should provide the following information, where applicable:
- Accession codes, unique identifiers, or web links for publicly available datasets
- A list of figures that have associated raw data
- A description of any restrictions on data availability

The cryo-EM maps and structure coordinates of GluN1-GluN2A and GluN1-GluN2B receptors were deposited in the Electron Microscopy Data Bank under accession numbers of EMD-31308 and EMD-31309, and in the Protein Data Bank under accession numbers of 7EU7 and 7EU8, respectively. The structure of S-ketamine and R-ketamine were accessible from the PubChem database under compound CID of 182137 and 644025, respectively. The human missense mutation c.1925T>G

(L642R) in grin2a gene was accessible from the ClinVar database under variation ID of 985631. Additional data that support the findings of this study are available from the corresponding author upon request.

Field-specific reporting

Please select the one below that is the best fit for your research. If you are not sure, read the appropriate sections before making your selection.

☒ Life sciences   ☐ Behavioural & social sciences   ☐ Ecological, evolutionary & environmental sciences

For a reference copy of the document with all sections, see nature.com/documents/nr-reporting-summary-flat.pdf

Life sciences study design

All studies must disclose on these points even when the disclosure is negative.

Sample size	Sample sizes were chosen as a maximum possible while considering practical limitations for data collection and subsequent data processing. 3D reconstructions were calculated from 6,214 images (615,863 particles) for GluN1-GluN2A receptor, 5,649 images (542,103 particles) for GluN1-GluN2B receptor collected in separate imaging sessions. These are sample sizes typically used to obtain high resolution cryo-EM structures of NMDA receptors. TEVC recordings were repeated at least three times on different Xenopus oocytes. The sample sizes of all these experiments were determined based on the consistency and variability.
Data exclusions	Data was excluded during cryo-EM data processing by removing 2D and 3D classes that did not possess high-resolution features, a standard procedure during the cryo-EM structural determination.
Replication	All attempts at replication were successful. Cryo-EM related experiments including purification, SDS-PAGE gel were reproduced three times independently. Electrophysiology experiments were repeated at least on three different Xenopus oocytes. Ligand binding assay were performed with triplicate measurements.
Randomization	Particles/images were randomly partitioned for resolution and quality assessment. Randomization serves no purpose in electrophysiological experiments.
Blinding	For ligand-binding assay, the experimentalists were blinded with the samples involved for subjective assessments. Blinding would serve no purpose for cryo-EM analysis, MD simulation and electrophysiological experiments.

Reporting for specific materials, systems and methods

We require information from authors about some types of materials, experimental systems and methods used in many studies. Here, indicate whether each material, system or method listed is relevant to your study. If you are not sure if a list item applies to your research, read the appropriate section before selecting a response.

Materials & experimental systems

n/a	Involved in the study
☒ ☐	Antibodies
☐ ☒	Eukaryotic cell lines
☒ ☐	Palaeontology and archaeology
☒ ☐	Animals and other organisms
☒ ☐	Human research participants
☒ ☐	Clinical data
☒ ☐	Dual use research of concern

Methods

n/a	Involved in the study
☒ ☐	ChIP-seq
☒ ☐	Flow cytometry
☒ ☐	MRI-based neuroimaging

Eukaryotic cell lines

Policy information about cell lines

Cell line source(s)	The sf9 insect cells and HEK293S GnTI– cells were general gifts from the laboratory of Prof.Eric Gouaux.
Authentication	The cells were routinely maintained in our laboratory. They were not authenticated for these studies.
Mycoplasma contamination	The cell lines were tested negative for mycoplasma contamination.
Commonly misidentified lines (See ICLAC register)	No commonly misidentified cell lines were used.